Next Materials 8 (2025) 100862

Contents lists available at ScienceDirect

Next Materials

journal homepage: www.sciencedirect.com/journal/next-materials

Research article

A DFT investigation on bi-functional {1 2 1} faceted orthorhombic $\beta-Sb_2O_3$ for water splitting application

Harshada A. Barve [a,b], Rupali R. Deshmukh [b], Zeenat A. Shaikh [a], Balaji G. Ghule [c], Shoyebmohamad F. Shaikh [d], Ji-Hyun Jang [c,*], Rajaram S. Mane [a,*], Krishna Chaitanya Gunturu [b,*]

[a] School of Physical Sciences, Swami Ramanand Teerth Marathwada University, Nanded, Maharashtra 431606, India
[b] School of Chemical Sciences, Swami Ramanand Teerth Marathwada University, Nanded, Maharashtra 431606, India
[c] School of Energy and Chemical Engineering, Department of Energy Engineering, School of Carbon Neutrality, School of Semiconductor Materials and Devices Engineering, UNIST, Ulsan 44919, Republic of Korea
[d] Department of Chemistry, College of Science, King Saud University, P.O. Box 2455, Riyadh 11451, Saudi Arabia

ARTICLE INFO

Keywords:
Antimony oxide
Density functional theory
Bi-functional catalyst
Oxygen evolution reaction
Hydrogen evolution reaction

ABSTRACT

An investigation into the bi-functional nature of the {1 2 1} plane of β-Sb_2O_3 during water splitting reactions is conducted using density functional theory calculations, examining oxygen evolution reaction (OER) and hydrogen evolution reaction (HER). The facet's asymmetric geometry and distorted electronic density create active sites that facilitate efficient adsorption of H_2O and reaction intermediates during catalytic reaction kinetics. The band structure and density of states (DOS) analysis using the HSE06 functional confirms the presence of lone pairs at metal ions near the valence band maximum, inducing an asymmetric charge distribution across the surface. The OER and HER mechanisms on {1 2 1} faceted orthorhombic $\beta-Sb_2O_3$ are further elucidated using binding energies, adsorption energies, and overpotential details at GGA-PBE as well as GGA-PBE-D3 level of theory. The identification of distinct active sites for OER and HER, further the moderate and excellent calculated lower overpotentials of 1.08 V and 0.11 V for OER and HER processes respectively, underscores the potential of {1 2 1} faceted orthorhombic β-Sb_2O_3 as a bifunctional electrocatalyst in the technology used for overall water splitting.

1. Introduction

In recent years, due to unique optical and optoelectronic properties, there has been a surge in the Sb_2O_3-based micro- or nanomaterials [1]. Antimony (III) oxide (Sb_2O_3) is a group V- VI semiconductor that naturally known to exhibit two crystalline polymorphs namely; a low–temperature cubic phase α-Sb_2O_3 (senarmontite) and a high–temperature orthorhombic phase β-Sb_2O_3 (valentinite). In the later stage, another high temperature polymorph i.e. γ-Sb_2O_3 has also come into existence. Structural distortions are associated with the lone pair of electrons localized to the Sb(III) ions which creates an asymmetric charge distribution in the bulk [2]. Due to a large optical non-linearity, high refractive index as well as good mechanical, thermal, and chemical durability, the as-synthesized antimony−based glasses are being used in ultra-fast optical switches, photosensitive materials [3,4], and as a flame retardant and smoke suppressant in combination with other composites in the polymer for coatings [5,6]. They have served as anode materials for sodium-ion, and lithium-ion batteries [7,8]. Catalytic nitrogen reduction [9] and CO_2 reduction [10] studies, recorded in the literature, are known for its wide applicability. The awakening environmental concerns and escalating needs for sustainable forms of energy are leading to the consideration of hydrogen as an ultimate substitute for traditional fossil fuels. The process of catalytic water splitting *via* either electrocatalysis or photocatalysis is the simplest and most feasible way to produce hydrogen and molecular oxygen. To improve the production of green sustainable energy, persistent efforts are being conducted to discover an efficient catalyst [11–13]. Over the past few years, Sb_2O_3 has increasingly been employed as a catalyst for electro-catalytic applications. Due to proper electronic band levels alignment to construct heterostructure, Sb_2O_3 nanostructures are found to be coupled with TiO_2 [14], and WO_3 [15], which, in turn, ameliorates catalytic activity for dye degradation. The as-synthesized $SrZrO_3-Sb_2O_3$ [16] heterostructure has

* Corresponding authors.
E-mail addresses: clau@unist.ac.kr (J.-H. Jang), rajarammane70@srtmun.ac.in (R.S. Mane), kc.gunturu@srtmun.ac.in (K.C. Gunturu).

https://doi.org/10.1016/j.nxmate.2025.100862
Received 18 January 2025; Received in revised form 3 June 2025; Accepted 17 June 2025
Available online 24 June 2025

endowed an improved hydrogen evolution.

To date, numerous approaches have been reported for the experimental synthesis of the Sb_2O_3 nanomaterials, targeting the applications mentioned earlier. Despite the synthesis progress, theoretical investigations into the electronic and structural properties of the Sb_2O_3 and further intermediates for catalytic water splitting on its surface are relatively scarce. Various crystalline polymorphs of antimony oxides such as the Sb_2O_3, Sb_2O_4, Sb_2O_5 have been studied for their electronic structures at the bulk level [17]. Wang *et al.* experimentally predicted the orthorhombic phase of pure $\beta-Sb_2O_3$ as a thermodynamically suitable anode material for water oxidation [18]. Although, the crystal structure of orthorhombic $\beta-Sb_2O_3$ was investigated decades ago [19], these studies were confined to bulk properties [20,21], overlooking the surface-level characteristics. These studies came out with interesting findings that the $\beta-Sb_2O_3$ holds *p*-type conductivity along with robust *n*-type character. Thus, the current study is motivated to explore the surface-level electronic structure of phase pure $\beta-Sb_2O_3$ for its potential use in electro-catalytic applications through material-intermediate interactions.

From previous reports, X-ray diffraction analysis confirmed that {1 2 1} facet with a minimum surface energy is assigned to maximum abundance over other faces [22-24]. The primary purpose of this investigation is to analyze the structural and electronic properties of the thermodynamically stable {1 2 1} facet of the $\beta-Sb_2O_3$ for a potential electro-catalytic water splitting applications. It includes a comprehensive exploration to thoroughly probe the different active sites present on the {1 2 1} surface of the $\beta-Sb_2O_3$, as well as their impact on the oxygen evolution reaction (OER) and hydrogen evolution reaction (HER) activities. Also, we include the surface Pourbaix diagrams to probe the most favorable degree of absorption of O*, OH*, and H* on {1 2 1} faceted $\beta-Sb_2O_3$.

2. Theoretical approach and computational details

2.1. Total energy calculation

All the calculations were performed using the density functional theory (DFT) as implemented in the Vienna *ab-initio* simulation package (VASP), version 6.1.2 [25]. To describe electron-ion interaction, the Kohn-Sham (KS) equations were solved using the projector augmented wave (PAW) method [26], employing a set of pseudo-potentials and plane waves to expand electronic wave functions. The KS orbitals were expanded in the plane-wave basis set with cut-off energy of 400 eV. For all geometry optimizations, the generalized gradient approximation (GGA) Perdew-Burke-Ernzerhof (PBE), as well as PBE with Grimme D3 van der Waals (vdW) dispersion corrections (GGA-PBE-D3) were chosen as exchange correlation functionals [27,28]. For the surface calculations, four layers of {1 2 1} facet of the orthorhombic $\beta-Sb_2O_3$ were sliced from the bulk. The simple monoclinic cell of $14.4485 \times 7.3081 \times 32.0292\ \AA$, for slab {1 2 1} contains 80 atoms of which 32 atoms of Sb and 48 atoms of O. A vacuum layer of 20 Å has been incorporated in the Z-direction of this supercell to avoid interaction between two successive periodic images. All calculations were spin polarized. The Brillouin zone integration was performed using the $1 \times 2 \times 1$ Monkhorst-Pack grid for geometry optimization while the larger grid of $3 \times 5 \times 1$ was used for density of states (DOS) calculation. For band structure calculation, a *k*-path along high symmetry points was chosen. The electronic properties of the surface including DOS and band structure were computed using the GGA-PBE as well as hybrid exchange-correlation functional HSE06 [29,30] with standard parameters, employed through single point calculations using PBE optimized geometry. A convergence energy threshold of 10^{-6} eV was employed in the self-consistent field calculations. The maximum Hellmann-Feynman force for each ionic optimization step was 0.05 eV/ Å. The Sb, O, and H atoms were treated with valence configuration of $5\,s^2 5p^3$ for Sb's (5 valence electrons), $2\,s^2 2p^4$ for O's (6 valence electrons), and 1*s* for H (1 valence electron). All the structural figures, along with partial charge density, were generated using the VESTA package [31].

2.2. The water splitting reaction

The overall water splitting reaction is as follows.

$$H_2O(l) \rightarrow H_2(g) + \frac{1}{2}O_2(g) \tag{1}$$

It consists of two half reactions. In the one half reaction, oxygen evolves at the anode and the other half reaction is hydrogen evolution reaction appears at the cathode.

2.2.1. Oxygen evolution reaction

The widely accepted OER mechanism consists of two water molecules which are split into four protons and an oxygen molecule with the release of four electrons [32,33]. The following reaction mechanisms take place under an acidic environment.

$$H_2O + {}^* \rightarrow HO^* + H^+ + e^- \tag{2}$$

$$HO^* \rightarrow O^* + H^+ + e^- \tag{3}$$

$$O^* + H_2O \rightarrow HOO^* + H^+ + e^- \tag{4}$$

$$HOO^* \rightarrow {}^* + O_2 + H^+ + e^- \tag{5}$$

The '*' denotes the substrate, where HO^*, O^*, and HOO^* are OER intermediates i.e., adsorbed HO, O, and HOO as coordinately unsaturated sites (CUS) on {1 2 1} facet of the $\beta-Sb_2O_3$. The process of water decomposition under standard conditions can be initiated by applying an external potential of 1.23 V. The variation in OER activity is explained in the form of free energy change 'ΔG', one of the intermediate steps along the OER reaction. From previous work [32–34], the expression for Gibbs' free energy change at standard conditions ($pH = 0$, and $T = 298.15$ K) for each intermediate step follows the following reactions.

$$\Delta G_1 = \Delta E_{HO^*} + (\Delta ZPE - T\Delta S)_1 - eU \tag{6}$$

$$\Delta G_2 = \Delta E_{O^*} - \Delta E_{HO^*} + (\Delta ZPE - T\Delta S)_2 - eU \tag{7}$$

$$\Delta G_3 = \Delta E_{HOO^*} - \Delta E_{O^*} + (\Delta ZPE - T\Delta S)_3 - eU \tag{8}$$

$$\Delta G_4 = 4.92 - \Delta E_{HOO^*} + (\Delta ZPE - T\Delta S)_4 - eU \tag{9}$$

In the above reactions, ΔE_{HO^*}, ΔE_{O^*}, and ΔE_{HOO^*} are the DFT binding energies of the single adsorbed HO, O, and HOO species, respectively. U is the external applied potential. The ΔZPE is a change in zero-point energies, T is the temperature ($T = 298.15$ K) and ΔS is entropic change. The ΔZPE and $T\Delta S$ values were calculated using computed vibrational frequencies and standard thermodynamic data. More details for determining free energies with entropic corrections (Table S1 and S2) are given in supporting information. The magnitude of the potential-determining step is a crucial factor which is deduced from the free energy diagram. Moreover, the size of the potential-determining step (G^{OER}) is the measurement of catalytic performance. This is the largest step at $U = 0$ or the last step which becomes downhill in the free energy diagram, and occurs as the potential (U) rises.

$$G^{OER} = \max\left[\Delta G_1, \Delta G_2, \Delta G_3, \Delta G_4\right] \tag{10}$$

To calculate G^{OER}, ΔG_{1-4} is considered at $U = 0$. As for the ideal catalyst, all the reaction free energies become zero at equilibrium potential i.e., 1.23 V. The theoretical overpotential (η^{OER}) for OER at standard conditions is then calculated as given in Eq. (11)

$$\eta^{OER} = (G^{OER}/e) - 1.23 \quad V \tag{11}$$

The binding energies of the intermediates HO^*, O^*, and HOO^* adsorbed on {1 2 1} facet of the $\beta-Sb_2O_3$ were calculated using the following expressions.

$$\Delta E_{HO^*} = E_{HO^*} - E_* - (E_{H_2O} - \frac{1}{2}E_{H_2}) \quad (12)$$

$$\Delta E_{O^*} = E_{O^*} - E_* - (E_{H_2O} - E_{H_2}) \quad (13)$$

$$\Delta E_{HOO^*} = E_{HOO^*} - E_* - (2E_{H_2O} - \frac{3}{2}E_{H_2}) \quad (14)$$

For which E_*, E_{HO^*}, E_{O^*}, and E_{HOO^*} are the DFT energies of a clean surface (*) and of surfaces with the single adsorbed species HO, O, and HOO, respectively. While the E_{H_2O}, and E_{H_2} are the ground state energies of H_2O and H_2 in the gaseous state, respectively.

2.2.2. Hydrogen evolution reaction

Catalytic HER is a two-step heterogeneous catalytic reaction, taking place on the surface of the cathode [35].

$2H^+ + 2e^- + {}^* \rightarrow H^* + H^+ + e^- \rightarrow H_2(g)$ (15)

Evaluation of the activity trend indicates that the adsorption energy of hydrogen atoms inherently governs the free energy of the HER process. The adsorption energy for hydrogen (E_{ads}^{H*}) was obtained from the DFT calculations at 0 K relative to gas phase H_2 molecule which is defined as in Eq. (16)

$$E_{ads}^{H^*} = E_{H^*} - E_* - \frac{1}{2}E_{H_2(g)} \quad (16)$$

where, E_{H^*} and E_* are the energy of the surface slab with and without atomic H adsorption, respectively and $E_{H_2(g)}$ is the total energy of the H_2 molecule in the gas phase. At the standard condition, the free energy change of adsorbed H was calculated from $\Delta G_{H^*} = E_{ads}^{H*} + (\Delta ZPE - T\Delta S)$ which is

$$\Delta G_{H^*} \approx E_{ads}^{H*} + 0.20\ eV \quad (17)$$

The theoretical overpotential (η^{HER}) for the HER at standard condition is then calculated as given in Eq.18.

$$\eta^{HER} = (\Delta G_{H^*}/e) \quad V \quad (18)$$

Adsorption energies for water molecule ($E_{ads}^{H_2O*}$) adsorbed on the catalyst surface were calculated from Eq.19.

$$E_{ads}^{H_2O*} = E_{H_2O/slab} - E_{H_2O} - E_{slab} \quad (19)$$

where, $E_{H_2O/slab}$, E_{H_2O}, and E_{slab} denote the DFT energies for H_2O adsorbed on slab, H_2O molecule, and clean slab respectively.

2.2.3. Construction of surface Pourbaix diagrams

Thermodynamically driven surface adsorptions and the most preferred adsorbed state of the catalyst can be analyzed by constructing surface Pourbaix diagrams. In aqueous electrolytes, it is assumed that only hydrogen, hydroxyl, and oxygen species can be exchanged between the electrolyte and catalyst surface [36]. A generalized representation of the adsorbed intermediates (O_mH_n*) and (H_n*) are written as,

$$^* + mH_2O \rightleftharpoons O_mH_n{}^* + (2m-n)(e^- + H^+) \quad (20)$$

$$n(e^- + H^+) + {}^* \rightleftharpoons H_n{}^* \quad (21)$$

The number of oxygen and hydrogen atoms is represented by m and n respectively on the adsorbate. We consider theoretical standard hydrogen electrode (SHE) [37] for modeling electrochemical reactions which states the equilibrium relation $H^+ + e^- \rightleftharpoons \frac{1}{2}H_2$. From this, the Gibbs' free energy change is . For solvated proton, k_B is Boltzmann's constant and T is the temperature, ($T = 298.15$ K). . In this work, we also neglect the electric field. The generalized expressions for Gibbs' free energy of (O_mH_n*) and (H_n*) computation are as follows

$$\Delta G = E_{O_mH_n{}^*} + (2m-n)\left(\frac{1}{2}E_{H_2} - eU_{SHE} - 0.0591pH\right) - E_* - mE_{H_2O} \quad (22)$$

$$\Delta G = E_{H_n{}^*} - n\left(\frac{1}{2}E_{H_2} - eU_{SHE} - 0.0591pH\right) - E_* \quad (23)$$

E_*, $E_{O_mH_n{}^*}$, $E_{H_n{}^*}$, E_{H_2}, and E_{H_2O} are the DFT energies of the clean surface, adsorbed O_mH_n*, H_n*, hydrogen molecule, and water molecule respectively. The generalized equations for the adsorption energies of oxygenated (O_mH_n*) and hydrogenated (H_n*) intermediates are given below

$$\Delta E_{O_mH_n{}^*} = E_{O_mH_n{}^*} - E_* - mE_{H_2O} + (2m-n)\left(\frac{1}{2}E_{H_2}\right) \quad (24)$$

$$\Delta E_{H_n{}^*} = E_{H_n{}^*} - E_* - n\left(\frac{1}{2}E_{H_2}\right) \quad (25)$$

Hence, for the construction of the surface Pourbaix diagram, we use the following expressions of the free energy changes, which are functions of pH and the electrode potential.

$$\Delta G = \Delta E_{O_mH_n{}^*} + (\Delta ZPE - T\Delta S) + (2m-n)(-eU_{SHE} - 0.059pH) \quad (26)$$

$$\Delta G = \Delta E_{H_n{}^*} + (\Delta ZPE - T\Delta S) + n(eU_{SHE} + 0.059pH) \quad (27)$$

3. Results and discussion

3.1. The geometry of {1 2 1} faceted $\beta-Sb_2O_3$

For the orthorhombic phase of the Sb_2O_3, {1 2 1} facet is thermodynamically most stable and of a low-index surface of β phase. Thereby, it is selected for surface investigation in the present work. Fig. 1a shows the geometry for bulk orthorhombic $\beta-Sb_2O_3$. The structure consists of infinite chains of the Sb_2O_3 stacked ladder-like structures running antiparallel to each other. Geometrically, each O is bounded between two Sb-ions in a bent manner, while each Sb is connected to three O ions.

From this bulk $\beta-Sb_2O_3$, the stable surface is cleaved along the {1 2 1} plane as shown in Fig. 1b. While performing surface termination, different symmetric terminations are possible along {1 2 1} direction at various cleavage positions. From the calculated surface free energies for Bi_2O_3, the stoichiometric symmetric terminations are most stable [38]. Similarly, for $\beta-Sb_2O_3$, among all possible terminations, only two slabs are stoichiometrically feasible i.e., the atomic ratio of Sb to O in the calculated unit cell is 2:3, following the formula Sb_2O_3. The other terminations are excess in either Sb or O, found non-stoichiometric, and discarded from this study. Hence, the stoichiometric termination surface with the lowest energy is considered between two possible slabs. Fig. 1c shows a four-layer {1 2 1} faceted symmetric slab model before and after geometry optimization. The outer layer of the surface is mainly composed of two coordinated O ions. Concerning the symmetry of the slab, a similar geometrical pattern has been found at the bottom layer. Amongst all Sb ions, 26 are found at three coordination sites (Sb3c) while 3 are at two coordination sites (Sb2c) on each surface layer (top and bottom). After geometry optimization, the atomic surface underwent relaxation with a minor degree of reconstruction. Some of the O atoms with dangling bonds tend to form bonds with nearby two coordinated Sb2c ions. Hence, all two coordinated Sb ions (Sb2c) become like three coordinated bonding structures. However, in newly bonded O with Sb2c, the bond length is elongated (2.03–2.07 Å) than with previously bonded O atoms (1.96–1.99 Å), reflecting the stronger bonding for previously bonded O atoms than that of newly bonded (see supporting information Table S4). There are negligible changes in bond lengths after adding D3 dispersion correction to GGA-PBE. To be noted, two of the three Sb2c centers have two such short bonds and one longer

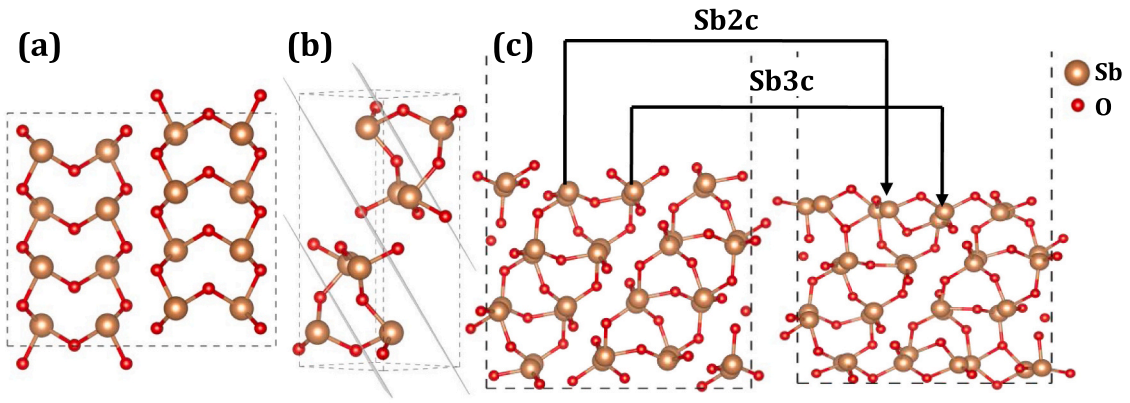

Fig. 1. Pictorial presentation showing; (a) bulk β−Sb_2O_3, (b) {1 2 1} surface cleavage in bulk β−Sb_2O_3, and (c) before and after geometry optimization for {1 2 1} faceted β−Sb_2O_3. Sb and O are represented by golden and red color balls respectively.

Sb−O bond while the third center has two longer and one short Sb−O bonds at the surface. On the other hand, the remaining Sb3c centers on the surface are observed with longer Sb−O bonds and one amongst them has elongated Sb−O bonds around 2.25 Å. This bonding distortion on the surface has been extended to the respective connecting Sb(III) ions within the next inner layer while all the metal ions are found as Sb3c bonding pattern. This enables a cohesive asymmetric coordination environment on the surface that leads to variations in electronic structure which offers new active sites on the surface for electro-catalytic activity.

3.2. Active sites analysis

To comprehend the asymmetric bonding on the surface, Bader charge analysis has been carried out for {1 2 1} β−Sb_2O_3 at GGA-PBE as well as PBE-D3 level of theory (Table S5). As compared to the bulk, the surface shows some interesting properties due to the presence of disparity in the bonding pattern around metal ions. Although, we have

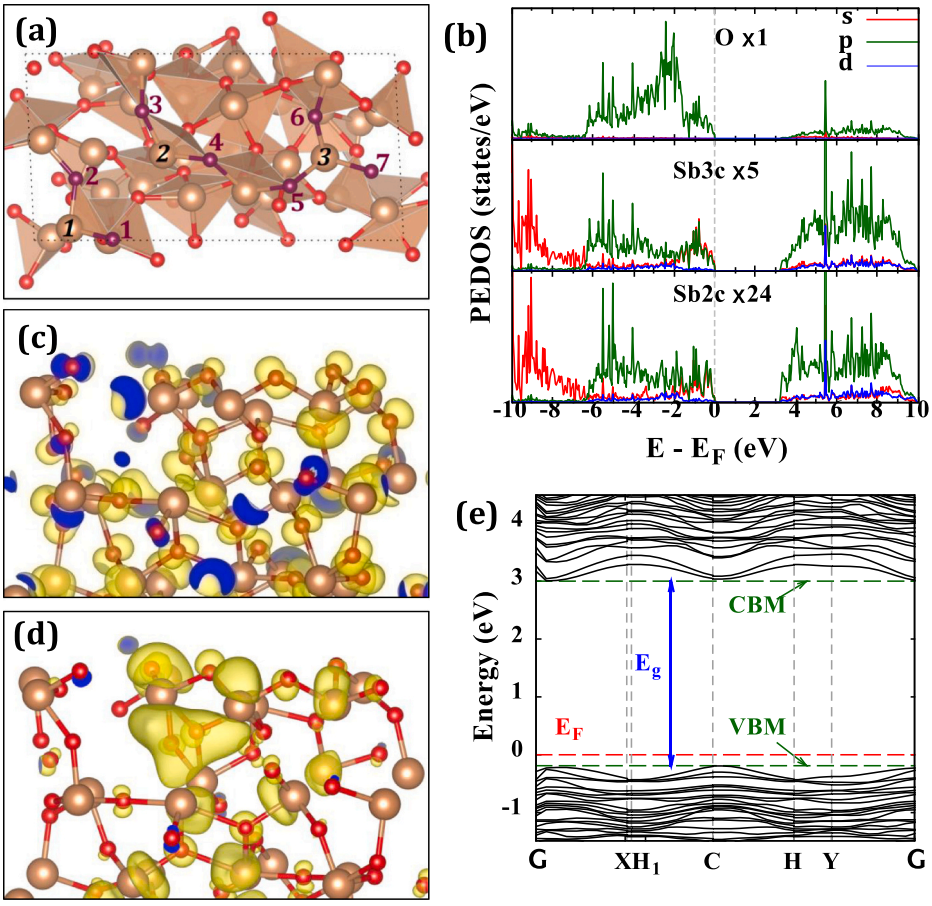

Fig. 2. {1 2 1} faceted β−Sb_2O_3 showing; (a) all coordinately unsaturated sites at the top surface for Sb (CUS_{Sb}) and O (CUS_O) available for adsorption. Golden, red, and brown represent Sb, O_{bulk}, and $O_{surface}$, respectively, (b) PEDOS for all Sb2c, Sb3c, and O ions at magnification factors of 24, 5, and 1, respectively. Partial charge density plots for; (c) VBM, and (d) CBM, with an isosurface level of 0.001, and yellow, and blue denoting the isosurface and its slicing due to cell boundary. (e) Electronic band structure of {1 2 1} facet of the β−Sb_2O_3 obtained by VASPKIT tool [39], calculated with HSE06 functional.

seen that Sb2c is reconstructed after optimization as Sb3c, Bader charges for previously known Sb2c are significantly different from the actual Sb3c, specifying the distinctive coordination environment of Sb(III) ions. It is observed that each Sb2c ion has a lower Bader charge of 1.70 e compared to other Sb3c ion, which is relatively more electropositive.

It resembles that, on the surface, Sb2c ions have donated fewer charges compared to other Sb3c, and hence specifically these less electropositive sites have more probability for adsorption of intermediates as they possess more electron density to interact. Additionally, this metal charge distortion and unsaturated bonding affects the nearby oxygens' environment at the surface. Hence, as labeled in Fig. 2a, this coordinately unsaturated antimony sites, CUS_{Sb}-1, CUS_{Sb}-2, and CUS_{Sb}-3 (golden balls) along with surface oxygen sites (brown balls), CUS_O-n (n = 1–7) are considered as active sites for catalytic OER and HER calculations.

3.3. Electronic density of states

The bonding interactions are further assessed through Fig. 2b by discussing the projected electronic density of states (PEDOS) distribution for {1 2 1} facet of the $\beta-Sb_2O_3$, computed using HSE06 functional. The contributions of states at valence band maximum (VBM) and conduction band minimum (CBM) are found similar to GGA-PBE functional results and the nature of DOS remains unchanged (supporting information Figure S3). The VBM is mainly composed of O 2*p* states with minor contributions from Sb 5*p* and 5*s* states. This kind of mixing at VBM, between metal *s* and *p* states with anion *p* states results from Sb−O anti-bonding interactions and is responsible for characteristic lone pair formation at metal centers [40–43]. The Sb(III) ions' presence with lone pairs at metal centers and geometrical distortion due to Sb3c and Sb2c centers provide supporting evidence for *p*-type conducting properties of the $\beta-Sb_2O_3$ [44–48].

Simultaneously, Sb 5*s* states are predominant while the minor contribution from O sp states at the bottom of the valence band below −6 eV resembles the strong Sb−O bonding nature. Due to the coordination variation for Sb3c and Sb2c ions, relative to 5*p* states, 5*s* states of the former are contributing more than the latter in VB maximum. The CBM is significantly composed of empty states of the Sb 5*p*, along with little contribution from the O 2*p* states. Here, the Fermi level is aligned to zero.

3.4. Partial charge density

Figs. 2c, and 2d depict the partial charge densities of {1 2 1} faceted $\beta-Sb_2O_3$ for VBM and CBM, respectively. In the case of VBM, the charge density contour is visible on oxygen along with Sb ion contributions from *p* and *s* orbitals. Similarly, for CBM, hybridization of empty orbitals of Sb 5*p* and O 2*p* states is observed, indicating extended electron delocalization between Sb and O ions. To be noted, the Sb2c centers that are identified as Sb active centers have distinct variations in terms of charge density distribution in VBM (Fig. 2c). The $CUS_{Sb}-1$ and $CUS_{Sb}-2$ possess negligible charge density in contrast to $CUS_{Sb}-3$, where anti-bonding hybrid orbital charge density is largely populated. However, in Fig. 2d, the charge density distribution in CBM also varies significantly such that, the charge density at $CUS_{Sb}-2$ is larger than that of $CUS_{Sb}-3$, and both are notably greater than that of $CUS_{Sb}-1$. Thus, despite their geometrical similarities and thereby, all $CUS_{Sb}-1$, $CUS_{Sb}-2$, and $CUS_{Sb}-3$ can behave differently during electro-catalytic response. Because of this charge distortion, nearby oxygen sites (CUS_O) also respond differently for intermediate adsorption during water splitting reactions.

3.5. Band structure and band gap

As GGA underestimates the band gap, the band structure depicted in Fig. 2e for the {1 2 1} $\beta-Sb_2O_3$ is calculated using HSE06 functional along high symmetry *k*-points. The broadening of VBM is attributed to the variation in the coordination environment of Sb(III) ions on the surface. Thus, the VBM and CBM are located on different symmetry points C and Γ at −0.20 eV and 3.01 eV, respectively to result in the indirect fundamental band gap of 3.21 eV.

The calculated band gap for the {1 2 1} $\beta-Sb_2O_3$ is alongside with the other stable metal oxide based electro-catalysts like TiO_2, ZnO, and SnO_2 with an estimated band gap in the range of 3.2–3.6 eV and which can further be modulated [49]. At the same time, the direct band gap located at symmetry points C and Γ is estimated to be 3.24 eV. Similar band structure but with a reduced band gap of 2.27 eV has been achieved at the GGA-PBE level of calculation (Figure S3 in SI). In addition, the inspection of the band structure accounts relatively more parabolic nature of the CBM than VBM. It also explores the fact further that the associated electron effective masses ($0.39m_e$) are smaller than the hole effective masses ($0.63m_e$) while both the quantities are close enough to the respective strong *p*-type and *n*-type metal oxides [17].

3.6. Electrocatalytic water splitting

3.6.1. Oxygen evolution reaction

As discussed in Section 3.2, metal as well as oxygen active sites are available at {1 2 1} facet of the $\beta-Sb_2O_3$. OER has been performed on coordinately unsaturated Sb active sites; $CUS_{Sb}-1$, $CUS_{Sb}-2$, and $CUS_{Sb}-3$ (Fig. 2a). The OER intermediates have had difficulty in adsorbing on the surface oxygen sites, hence, CUS_O is not considered for OER. Considering the OER intermediates HO*, O*, and HOO* visually adsorb at each Sb active site, and corresponding binding energies can be estimated using Eqs. (12)–(14).

Since each active site is surrounded by a different electronic environment, each active site is different and shows respective catalytic performance upon adsorption of OER intermediates. The water adsorption on the catalyst surface is the crucial step that initiates further intermediate reactions. Negative values of adsorption energies of H_2O^* (calculated using Eq.19), shown in Table 1, represent the feasibility of water adsorption on the surface of the catalyst. As there is no change in trend for the selectivity of active sites while addition of Grimme D3 dispersion correction to GGA-PBE, results mentioned here are computed by using GGA-PBE-D3 and corresponding values for GGA-PBE are reported in supporting information (see Table S6 and Table S7). The priority for strong H_2O adsorption on these active sites imitates $CUS_{Sb}-2 > CUS_{Sb}-1 > CUS_{Sb}-3$. Figure S4 shows the optimized geometries for a clean surface and each intermediate adsorbed at CUS_{Sb} on the {1 2 1} surface of the $\beta-Sb_2O_3$.

The changes in free energies are evaluated by using Eq.6−9 and have been constructed for OER intermediates for all active sites as illustrated in Fig. 3a and Figure S6. For all three sites, ΔG_3 has been identified as the potential–determining step, which is splitting of the second water molecule that can result in HOO* adsorption on the active site. All OER steps are exothermic above this potential. The corresponding theoretical overpotentials for all sites calculated using Eq.11 are included in Table 1. The lowest overpotential is found to be 1.08 V for $CUS_{Sb}-1$, which is in agreement with the previous results [50]. To be noted, despite strong and weak H_2O adsorption at $CUS_{Sb}-2$ and $CUS_{Sb}-3$ respectively, the moderate adsorbed active site $CUS_{Sb}-1$ has less overpotential. Norskov *et al.* [32] predicted that the oxygen evolution activity is limited by the HOO* formation step through a strong O* binding (< 2.3 eV) on the oxide surfaces. On the other hand, the binding energy for O* adsorption for efficient catalyst RuO_2 is 2.66 eV while, the same is evaluated for the {1 2 1} surface of the $\beta-Sb_2O_3$ is 2.27 eV. Moreover, this material also seems to follow the universal scaling relation between HO* and HOO* such that the difference of $\Delta E_{HOO^*} - \Delta E_{HO^*}$ is approximately 3.2 eV, demonstrating the potentiality of the Sb_2O_3 as a better OER catalyst. Table 2 depicts the comparison of the OER overpotential of β-Sb_2O_3 with frequently used metal oxide based catalysts that were found to be promising concerning its easy availability and synthesis

Table 1
Adsorption energies of H_2O ($E_{ads}^{H_2O*}$ in eV), distances between M−O_{H2O*}, distance M-X (M= Sb_{slab}, X = HO*, O*, HOO*) in Å, binding energies of HO*, O*, and HOO* (in eV) adsorbed on {1 2 1} facet of the β−Sb_2O_3 at distinct CUS_{Sb}, corresponding potential determining step (ΔG_{OER} in eV), and OER overpotential (in V) calculated using GGA-PBE-D3.

CUS_{Sb}	H_2O		HO*		O*		HOO*		ΔG_{OER}	η^{OER}
	M-O_{H2O*}	$E_{ads}^{H_2O*}$	M-HO*	ΔE_{HO*}	M-O*	ΔE_{O*}	M-HOO*	ΔE_{HOO*}		
1	2.55	−0.522	1.98	1.090	1.85	2.273	2.36	4.317	2.314	1.08
2	2.48	−0.542	1.98	0.888	2.05	1.396	2.01	4.091	2.965	1.74
3	2.29	−0.385	1.96	0.798	1.83	2.110	2.02	4.394	2.554	1.32

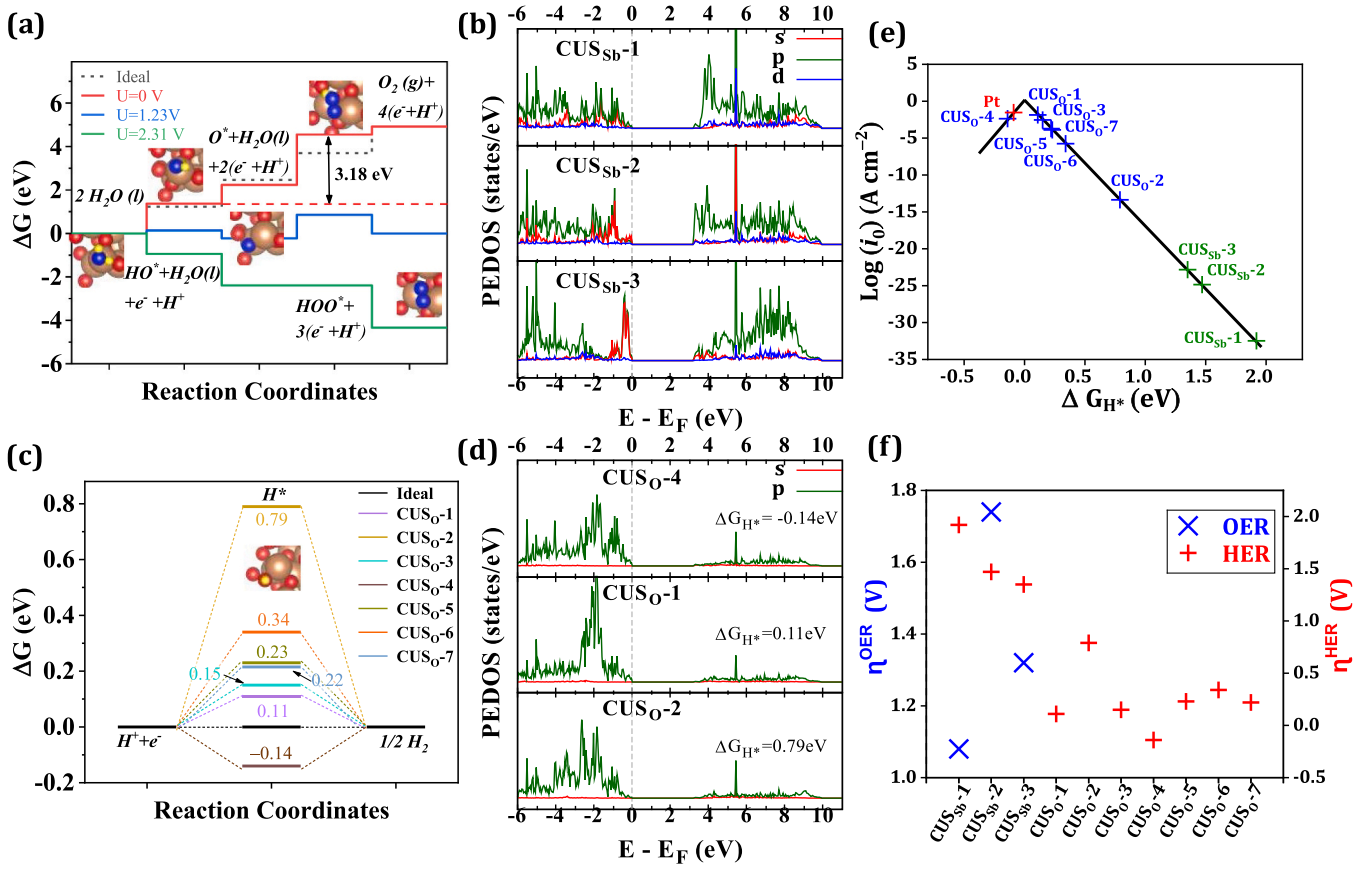

Fig. 3. (a) Free energy diagram for OER intermediates adsorbed at CUS_{Sb}−1 (η^{OER} = 1.08 V) and, (b) PEDOS for CUS_{Sb} active sites (c) Free energy diagram for HER showing H* adsorbed at CUS_O at PBE-D3 level (d) PEDOS for selected CUS_O active sites at HSE06 level of calculation on the {1 2 1} facet of the β−Sb_2O_3 (e) Volcano plot for HER, (f) Comparative OER and HER overpotentials.

Table 2
Comparative data showing OER overpotential of the β-Sb_2O_3 with other metal oxide catalysts.

Catalyst	XC Functional	η^{OER} (V)	Ref.
β-Sb_2O_3	PBE-D3	1.08	Present work
TiO_2	PBE	0.80 (rutile)	[51]
		1.04 (anatase)	
		1.15 (brookite)	
	RPBE	1.19 (rutile)	[34]
RuO_2	RPBE	0.37 (rutile)	[34]
IrO_2	RPBE	0.56 (rutile)	[34]
	PBE	0.96 (rutile)	[52]
WO_3	PBE	1.04–1.10	[53]
Fe_2O_3	PBE+U	0.79–1.47	[54]
Co_3O_4	RPBE+U	0.76	[55]
ZnO	PBE+U	1.04	[56]
Mn_3O_4	HSE06	0.84	[57]
δ-MnO_2	HSE06	0.78	[57]

protocols.

Fig. 3b illustrates that CUS_{Sb}-1 is distinctively different from the other two metal active sites. In support of the observations drawn from the PCD and DOS plots, in the case of CUS_{Sb}-1, there is a larger contribution of Sb-*p* states at VBM. On the other hand, CUS_{Sb}-3 has comparatively dominant contributions from both *s* and *p* states. While, relatively missing *p* states, at the same time contribution of *s* states seems to be significant in CUS_{Sb}-2 ascertaining the prominent role of Sb-*p* states over Sb-s states in attaining smaller overpotential in the OER process. It remains the overpotentials for metal active sites in order CUS_{Sb}-1 < CUS_{Sb}-3 < CUS_{Sb}-2 accordingly. It also overwhelms to conclude that increased overpotentials left the metal active sites to have a resemblance with other Sb 3c centers.

3.6.2. Hydrogen evolution reaction

Under the water splitting mechanism, HER performance on the {1 2 1} facet of the β−Sb_2O_3 has been evaluated at the surface Sb (CUS_{Sb}) and O (CUS_O) sites. Figure S5 presents the optimized geometry of hydrogen

(H*) adsorbed on the surface.

The adsorption energy of H* is the simple descriptor to estimate the catalytic activity for HER which was calculated using Eq.16. From adsorption energy, the change in free energy of H* for each active site has been evaluated through Eq.17 and plotted in Fig. 3c for CUS_O sites while Figure S8 includes CUS_{Sb} also. The Gibbs free energy of the intermediate state, $|\Delta G_H{}^*|$, was regarded as a major descriptor of the HER activity. A smaller $|\Delta G_{H^*}|$ represents high catalytic activity. According to the Sabatier principle, ΔG_{H^*} should be zero under ideal conditions, and from volcano plot analysis, comparatively weak adsorption of H* shall be presumed for $\Delta G_{H^*} > 0$ [58]. The H* should not bind with the active site too strongly or too loosely. If it binds too strongly then the release of the H_2 will be inhibited and even the HER process will be hindered if it binds too weakly. One more descriptor of the catalytic activity is the bond strength between the hydrogen and CUS. The bond strength is correlated to the energy level position of the bonding or anti-bonding orbital. Specifically, for strong bonding interaction, a bonding orbital with a low energy level or an anti-bonding orbital with a high energy level is predicted. The bond distance between adsorbed H* and Sb ions of the slab has been shown in Table 3. At CUS_{Sb}, ΔG_{H^*} values are relatively higher than ideal ΔG_{H^*} for instance 1.35 eV for CUS_{Sb}-3. Contrary, at surface oxygen sites CUS_O, observed ΔG_{H^*} values are lower enough i.e.0.11 eV and −0.14 eV, respectively for CUS_O-1 and CUS_O-4, which are close to the ideal $\Delta G_{H^*} = 0$ eV. Because of the charge delocalization of active metal sites to the nearby oxygen sites, CUS_O shows feasible H adsorption. The preference of CUS_O-1 and CUS_O-4 over other sites for HER activity has been supported by the PEDOS for CUS_O in Fig. 3d and Figure S5, which shows more contribution of *p*-states at VBM. Among all surface oxygen sites, the CUS_O-2 has been characterized with very less contribution from O-2*p* states in PEDOS (Fig. 3d), resulting in a higher free energy of 0.79 eV. Fig. 3e illustrates the volcano plot (exchange current $\log(i_0)$ as a function of hydrogen chemisorptions energy ΔG_{H^*}) for evaluation of HER performance which further supports our findings. An appropriate catalyst will be situated in a close proximity to the summit of the volcano plot when ΔG_{H^*} tends towards zero [59]. CUS_O-1 and CUS_O-4 are observed to be located near the peak of the volcano plot depicting comparable HER performance to the classical catalyst platinum. The theoretical overpotential for HER has been calculated using Eq.18. In agreement with our recent experimental studies and present DFT results, the HER overpotential of β-Sb_2O_3 is notably superior to similar metal oxide based catalysts as shown in Table 4. In conjunction with the calculated overpotentials for both OER and HER, (Fig. 3f) the {1 2 1} facet of the $\beta-Sb_2O_3$ has been evaluated as a bi-functional electrocatalyst for overall water splitting application.

3.7. Construction of surface Pourbaix diagrams

For the construction of the surface Pourbaix diagram, we have considered different monolayer coverage of H* (4 H, 2 H, and 1 H adsorption on oxygen sites), HO* (1/8, ¼, and ½ number of available metal sites), and O* (1/8, ¼, and ½ number of available metal sites) on the surface of $\beta-Sb_2O_3$. We have calculated the free energy of adsorbed species using Eqs. 26–27. Accordingly, Fig. 4a shows the relative stability of adsorbed species as a function of potential U_{SHE} at $pH = 0$. The line with the lowest free energy defines the most stable surface coverage at that potential. Fig. 4b shows the surface Pourbaix diagram as, a projection of the surface with lowest free energy in (U_{SHE}, *pH*, *G*) space down to the (*U*, *pH*) plane. The potential *vs.* theoretical reversible hydrogen electrode (*RHE*) defines $U_{RHE} = U_{SHE} + k_B T\, ln10\, p^H/e$. (At $pH = 0$, $U_{RHE} = U_{SHE}$). Adsorption energies of all adsorbed $O_mH_n{}^*$ and $H_n{}^*$ are given in Table S8. On {1 2 1} surface of $\beta-Sb_2O_3$, at $pH = 0$, for $U_{RHE} < -0.2$ V surface hydrogen begins to adsorb with increasing coverage of H* stabilized as potential decreases. For alkaline conditions, this potential takes more negative values ~below −0.6 V (*RHE*). Fig. 4b also depicts the surface adsorbed species attained stability with a slope of −0.0591 V/pH, for instance, at $pH = 0$, hydroxide adsorption with coverage of 1/4 ML is favorable above 0.43 V (*RHE*), and in alkaline environment this potential drop to 0.03 V(*RHE*). For acidic conditions, at 0.66 V (*RHE*) the HO* coverage increases to ½ ML OH while at $pH = 7$, this potential reduces to 0.27 V (*RHE*). Thus, the surface adsorptions over {1 2 1} faceted $\beta-Sb_2O_3$ have been envisaged for both HER and OER processes with a large degree of intermediate adsorption over the surface which has been anticipated for electrocatalytic water splitting application.

Table 3
Distances between X − H* (X = Sb, O) (in Å), adsorption energies (in eV), and respective overpotentials (in V) on the {1 2 1} faceted $\beta-Sb_2O_3$ at distinct active sites calculated using GGA-PBE-D3.

Active site		X − H*	ΔE_{H^*} (eV)	η^{HER} (V)
Sb	$CUS_{Sb}-1$	1.81	1.720	1.92
	$CUS_{Sb}-2$	1.74	1.272	1.47
	$CUS_{Sb}-3$	1.73	1.153	1.35
O	CUS_O-1	0.98	−0.092	0.11
	CUS_O-2	1.01	0.585	0.79
	CUS_O-3	0.98	−0.048	0.15
	CUS_O-4	0.98	−0.337	−0.14
	CUS_O-5	0.98	0.033	0.23
	CUS_O-6	0.98	0.138	0.34
	CUS_O-7	0.98	0.025	0.22

Table 4
Comparative data showing HER overpotential of the β-Sb_2O_3 with other metal oxide catalysts.

Catalyst	XC Functional	η^{HER} (V)	Ref.
β-Sb_2O_3	PBE- D3	0.11	Present work
WO_3	PBE	1.40 (W-site) −0.5 (O-site)	[60]
Bi_2O_3	PBE	0.94	[61]
MoO_2	PW91	0.15	[62]
IrO_2	PBE	−0.75	[63]
RuO_2	PBE	0.12	[64]
TiO_2	RPBE	−0.18 (Rutile) 0.28 (Monoclinic) 0.15 (Amorphous)	[65]
CeO_2	PBE+U	−1.25	[66]
MnO_2	PBE	−0.7	[67]
NiO	PBE	−0.64	[67]
Co_3O_4	PBE	−0.24	[24]

4. Conclusions

Upon moving from the bulk to the surface, the presence of weak or dangling bonds at the surface causes an asymmetric electronic structure that alters the adsorption kinetics distinctively. In the present work, the fundamental electronic investigation of the stoichiometric and stable {1 2 1} facet of the $\beta-Sb_2O_3$ has been performed by using DFT which has been known for both *p*-type and *n*-type conducting properties. For all intermediates adsorption, GGA-PBE, as well as GGA-PBE with Grimme D3 dispersion functional to treat vdW interaction between the cage structure of $\beta-Sb_2O_3$ have been employed. The calculated indirect band gap of 3.21 eV at the HSE06 level is found to be comparable to other metal oxide-based stable electrocatalysts and anticipated for water splitting application. Thus, there are 3 Sb active sites (CUS_{Sb}) and 7 O active sites (CUS_O) that come out with the surface for adsorption. OER intermediates adsorption desirable on metal sites only (CUS_{Sb}) while all the possible adsorption sites (CUS_{Sb} and CUS_O) are included for further adsorption of HER studies. The important step for water oxidation or reduction is the adsorption of H_2O on the {1 2 1} facet of the $\beta-Sb_2O_3$. Similar to other previously known catalysts, $\beta-Sb_2O_3$ also follows the scaling relationship between the binding energies of HO* and HOO* species. The overpotential for OER (1.08 V) claims that the formation of

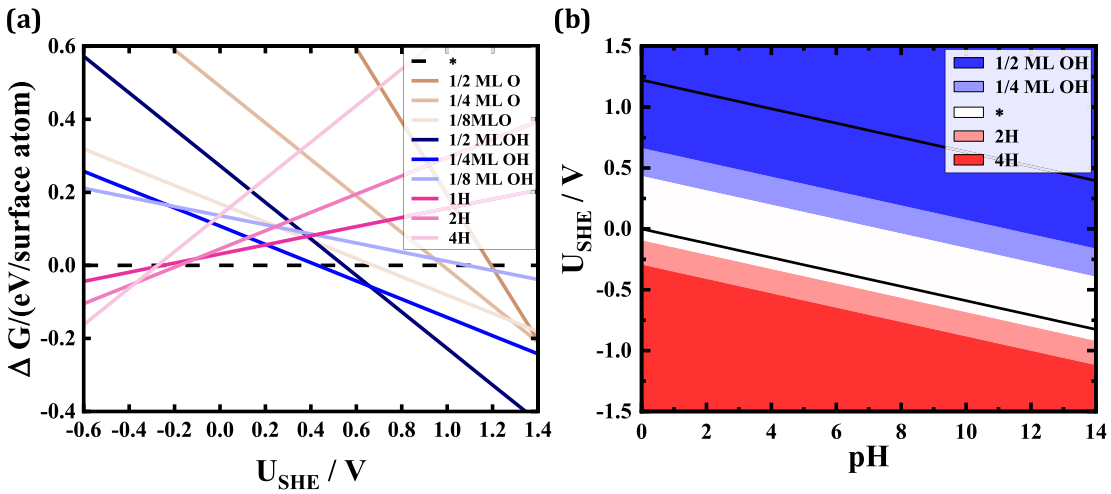

Fig. 4. (a) Stability of O*, HO*, and H* at pH= 0. (b) Surface Pourbaix diagram for on the {1 2 1} faceted $\beta-Sb_2O_3$ at PBE-D3 level of calculation. The black lines in (b) denote potentials of 1.23 V *vs.* RHE (OER potential) and 0 V *vs.* RHE (HER potential).

HOO* is the potential–determining step and found that CUS_{Sb}-1 is preferred over the other two active sites. On the other hand, HER on the {1 2 1} facet of $\beta-Sb_2O_3$ is demonstrated for the first time. During this study, the CUS_O sites possess relatively strong catalytic activity for HER compared to CUS_{Sb} sites. The lowest free energies calculated at CUS_O-1 and CUS_O-4 are 0.11 and −0.14 eV, respectively, close to the ideal value. The theoretically calculated overpotentials indicate that the OER activity is similar to the well-known, largely investigated, metal oxide OER catalyst TiO_2, which is 1.19 V [32]. Moreover, exceptional HER activity on the {1 2 1} faceted $\beta-Sb_2O_3$ shows its bi-functional catalytic performance for overall water splitting process. The PCD and PEDOS analyses elucidate that the significant contributions from Sb 5*p* and O 2*p* states in VBM, whilst Sb 5*p* states role has been attributed to attaining the required smaller overpotentials and distinctively different active sites for OER and HER during water splitting reactions. Also, we have constructed the surface Pourbaix diagram at potentials relevant for OER and HER, showing a relatively stable surface at corresponding potential and pH. These results are in agreement with our recently published experimental findings where 206 mV and 124 mV overpotentials for OER and HER are respectively obtained at 10 mA cm^2 with sustained stability [68]. Allen *et al.* [17] discussed previously that from smaller hole and electron effective masses, $\beta-Sb_2O_3$ may show both *p* and *n*-type semiconducting properties. Thus, this study reiterates through DFT analysis that the {1 2 1} faceted $\beta-Sb_2O_3$ can be behaved as both anode and cathode electrode materials for electrocatalytic water splitting applications. Accordingly, the bi-functional nature of the {1 2 1} faceted $\beta-Sb_2O_3$ during the water splitting process has been unveiled systematically.

CRediT authorship contribution statement

Harshada A. Barve: Methodology, Investigation, Writing-original draft. **Rupali R. Deshmukh:** Investigation. **Zeenat A. Shaikh:** Formal analysis. **Balaji G. Ghule:** Methodology, Data curation. **Shoyebmohamad F. Shaikh:** Resources, Formal analysis. **Ji-Hyun Jang:** Resources, Software, Writing- Reviewing and Editing. **Rajaram S. Mane:** Conceptualization, Writing- Reviewing and Editing. **Krishna Chaitanya Gunturu:** Conceptualization, Methodology, Software, Writing- Reviewing and Editing, Supervision.

Declaration of Competing Interest

The authors declare that they have no known competing financial interests or personal relationships that could have appeared to influence the work reported in this paper.

Acknowledgment

G.K.C. thanks CSIR, New Delhi, India for the financial assistance throughout this research project 01(3079)/21/EMR-II. RRD thanks CSIR, New Delhi, India for SRF support. The authors are thankful to the UNIST Supercomputing facility for providing computational support. The authors extend their sincere appreciation to the Researchers Supporting Project number (RSP2025R370) at King Saud University, Riyadh, Saudi Arabia, for their valuable financial support.

Appendix A. Supporting information

Supplementary data associated with this article can be found in the online version at doi:10.1016/j.nxmate.2025.100862.

Data availability

The data sets generated and/or analyzed in this study are available from the corresponding author upon reasonable request.

References

[1] I.L. Validžić, N.D. Abazović, M. Mitrić, M.V. Lalić, Z.S. Popović, F.R. Vukajlović, Novel organo-colloidal synthesis, optical properties, and structural analysis of antimony sesquioxide nanoparticles, J. Nanopart. Res. 15 (2013) 1347, https://doi.org/10.1007/s11051-012-1347-x.1347.

[2] A. Matsumoto, Y. Koyama, A. Togo, M. Choi, I. Tanaka, Electronic structures of dynamically stable As_2O_3, Sb_2O_3, and Bi_2O_3 crystal polymorphs, Phys. Rev. B 83 (2011) 214110, https://doi.org/10.1103/PhysRevB.83.214110.

[3] A.E. Ersundu, M. Çelikbilek, M. Baazouzi, M.T. Soltani, J. Troles, S. Aydin, Characterization of new Sb_2O_3-based multicomponent heavy metal oxide glasses, J. Alloy. Compd. 615 (2014) 712–718, https://doi.org/10.1016/j.jallcom.2014.07.024.

[4] M. Nalin, M. Poulain, S.J.L. Ribeiro, Y. Messaddeq, Crystallization study of the (1-x)Sb_2O_3-(x)$SbPO_4$ glass system, Mat. Chem. Phy. 112 (2008) 1069–1073, https://doi.org/10.1016/j.matchemphys.2008.07.033.

[5] M. Si, J. Feng, J. Hao, L. Xu, J. Du, Synergistic flame retardant effects and mechanisms of nano-Sb_2O_3 in combination with aluminum phosphinate in poly (ethylene terephthalate), Polym. Degrad. Stab. 100 (2014) 70–78, https://doi.org/10.1016/j.polymdegradstab.2013.12.023.

[6] H. Qu, W. Wu, Y. Zheng, J. Xie, J. Xu, Synergistic effects of inorganic tin compounds and Sb_2O_3 on thermal properties and flame retardancy of flexible poly (vinyl chloride), Fire Saf. J. 46 (7) (2011) 462–467, https://doi.org/10.1016/j.firesaf.2011.07.006.

[7] J. Pan, N. Wang, Y. Zhou, X. Yang, W. Zhou, Y. Qian, J. Yang, Simple synthesis of a porous Sb/ Sb_2O_3 nanocomposite for a high-capacity anode material in Na-ion batteries, Nano Res. 10 (2017) 1794–1803, https://doi.org/10.1007/s12274-017-1501-y.

[8] H. Bryngelsson, J. Eskhult, L. Nyholm, M. Herranen, O. Alm, K. Edström, Electrodeposited Sb and Sb/ Sb_2O_3 nanoparticle coatings as anode materials for Li-ion batteries, Chem. Mater. 19 (5) (2007) 1170–1180, https://doi.org/10.1021/cm0624769.

[9] S. Cao, Z. Guan, Y. Feng, H. Wang, R. Liu, K. Ding, S-doped Sb_2O_3 nanorods for electrocatalytic nitrogen reduction, ACS Appl. Nano Mater. 5 (2022) 3591–3598, https://doi.org/10.1021/acsanm.1c04177.

[10] Y. Li, S. Chu, H. Shen, Q. Xia, A.W. Robertson, J. Masa, U. Siddiqui, Z. Sun, Achieving highly selective electrocatalytic CO_2 reduction by tuning CuO- Sb_2O_3 nanocomposites, ACS Sustain. Chem. Eng. 8 (2020) 4948–4954, https://doi.org/10.1021/acssuschemeng.0c00800.

[11] S. Ye, R. Wang, M.-Z. Wu, Y.-P. Yuan, A review on g-C_3N_4 for photocatalytic water splitting and CO_2 reduction, Appl. Surf. Sci. 358 (A) (2015) 15–27, https://doi.org/10.1016/j.apsusc.2015.08.173.

[12] B. Hinnemann, P.G. Moses, J. Bonde, K.P. Jørgensen, J.H. Nielsen, S. Horch, I. Chorkendorff, J.K. Nørskov, Biomimetic hydrogen evolution: MoS_2 nanoparticles as catalyst for hydrogen evolution, J. Am. Chem. Soc. 127 (15) (2005) 5308–5309, https://doi.org/10.1021/ja0504690.

[13] T. Teusch, T. Klüner, Understanding the water splitting mechanism on WO_3(001)—a theoretical approach, J. Phys. Chem. C. 123 (46) (2019) 28233–28240, https://doi.org/10.1021/acs.jpcc.9b08268.

[14] D.-N. Liu, G.-H. He, L. Zhu, W.-Y. Zhou, Y.-H. Xu, Enhancement of photocatalytic activity of TiO_2 nanoparticles by coupling Sb_2O_3, Appl. Surf. Sci. 258 (20) (2012) 8055–8060, https://doi.org/10.1016/j.apsusc.2012.04.171.

[15] G.-H. He, C.-J. Liang, Y.-D. Ou, D.-N. Liu, Y.-P. Fang, Y.-H. Xu, Preparation of novel Sb_2O_3/WO_3 photocatalysts and their activities under visible light irradiation, Mater. Res. Bull. 48 (6) (2013) 2244–2249, https://doi.org/10.1016/j.materresbull.2013.02.055.

[16] A.M. Huerta-Flores, L.M. Torres-Martínez, E. Moctezuma, J.E. Carrera-Crespo, Novel $SrZrO_3$- Sb_2O_3 heterostructure with enhanced photocatalytic activity: band engineering and charge transference mechanism, J. Photochem. Photobiol. A Chem. 356 (2018) 166–176, https://doi.org/10.1016/j.jphotochem.2017.12.049.

[17] J.P. Allen, J.J. Carey, A. Walsh, D.O. Scanlon, G.W. Watson, Electronic structures of antimony oxides, J. Phys. Chem. C. 117 (28) (2013) 14759–14769, https://doi.org/10.1021/jp4026249.

[18] Y. Wang, L. Jiang, Y. Liu, D. Tang, F. Liu, Y. Lai, Facile synthesis and photoelectrochemical characterization of Sb_2O_3 nanoprism, J. Alloy. Compd. 727 (2017) 469–474, https://doi.org/10.1016/j.jallcom.2017.08.106.

[19] C. Svensson, The crystal structure of orthorhombic antimony trioxide, Sb_2O_3, Acta Crystallogr. Sect. B 30 (2) (1974) 458–461, https://doi.org/10.1107/S0567740874002986.

[20] M.H. Lakhdar, Y.B. Smida, M. Amlouk, Synthesis, optical characterization and DFT calculations of electronic structure of Sb_2O_3 films obtained by thermal oxidation of Sb_2S_3, J. Alloy. Compd. 681 (2016) 197–204, https://doi.org/10.1016/j.jallcom.2016.04.026.

[21] A. Jafari, B. Klobes, I. Sergueev, D.H. Moseley, M.E. Manley, R. Dronskowski, V. L. Deringer, R.P. Stoffel, D. Bessas, A.I. Chumakov, R. Rüffer, A. Mahmoud, C. A. Bridges, R.P. Herman, Phonon spectroscopy in antimony and tellurium oxides, J. Phys. Chem. A 124 (39) (2020) 7869–7880, https://doi.org/10.1021/acs.jpca.0c05060.

[22] K. Liu, J. Zhai, L. Jiang, Fabrication and characterization of superhydrophobic Sb_2O_3 films, Nanotechnology 19 (2008) 165604, https://doi.org/10.1088/0957-4484/19/16/165604.

[23] M. Abdellatif, Y. Louafi, D. Nunes, T. Freire, E. Fortunato, R. Martins, S. Kabouche, Studies on photocatalytic degradation of Rhodamine B using the valentinite Sb_2O_3, Reac Kinet. Mech. Cat. 136 (2023) 1643–1655, https://doi.org/10.1007/s11144-023-02411-1.

[24] J. Zhang, Q. Xu, J. Wang, Y. Li, H. Jiang, C. Li, Dual-defective Co_3O_4 nanoarrays enrich target intermediates and promise high-efficient overall water splitting, Chem. Eng. J. 424 (2021) 130328, https://doi.org/10.1016/j.cej.2021.130328.

[25] G. Kresse, furtmüllar, J. Efficient iterative schemes for ab initio total-energy calculations using a plane–wave basis set, Phys. Rev. B 54 (1996) 11169–11186, https://doi.org/10.1103/PhysRevB.54.11169.

[26] P.E. Blöchl, Projector augmented-wave method, Phy. Rev. B 50 (24) (1994) 17953–17979, https://doi.org/10.1103/PhysRevB.50.17953.

[27] J.P. Perdew, K. Burke, M. Ernzerhof, Generalized gradient approximation made simple, Phys. Rev. Lett. 77 (18) (1996) 3865–3868, https://doi.org/10.1103/PhysRevLett.77.3865.

[28] S. Grimme, J. Amntony, S. Ehrlich, H. Krieg, A consistent and accurate ab initio parametrization of density functional dispersion correction (DFT-D) for the 94 elements H-Pu, J. Chem. Phys. 132 (15) (2010) 154104, https://doi.org/10.1063/1.3382344.

[29] J. Heyd, G.E. Scuseria, M. Ernzerhof, Hybrid functionals based on a screened coulomb potential, J. Chem. Phys. 118 (2003) 8207–8215, https://doi.org/10.1063/1.1564060.

[30] J. Heyd, G.E. Scuseria, M. Ernzerhof, Erratum: "Hybrid functionals based on a screened Coulomb potential" [J. Chem. Phys. 118, 8207 (2003)], J. Chem. Phys. 124 (21) (2006) 219906, https://doi.org/10.1063/1.2204597.

[31] K. Momma, F. Izumi, VESTA 3 for three-dimensional visualizatin of crystal, volumetric, and morphology data, J. Appl. Crystallogr 44 (2011) 1272–1276, https://doi.org/10.1107/S0021889811038970.

[32] J. Rossmeisl, Z.-W. Qu, H. Zhu, G.-J. Kroes, J.K. Nørskov, Electrolysis of water on oxide surfaces, J. Electroanal. Chem. 607 (2007) 83–89, https://doi.org/10.1016/j.jelechem.2006.11.008.

[33] I.C. Man, H.-Y. Su, F. Calle-Vallejo, H.A. Hansen, J.I. Martínez, N.G. Inoglu, J. Kitchin, T.F. Jaramillo, J.K. Nørskov, J. Rossmeisl, Universality in oxygen evolution electrocatalysis on oxide, ChemCatChem 3 (2011) 1159–1165, https://doi.org/10.1002/cctc.201000397.

[34] Á. Valdés, Z.-W. Qu, G.-J. Kroes, J. Rossmeisl, J.K. Nørskov, Oxidation and photo-oxidation of water on TiO_2 surface, J. Phys. Chem. C. 112 (2008) 9872–9879, https://doi.org/10.1021/jp711929d.

[35] Y. Zhu, D. Zhang, L. Gong, L. Zhang, Z. Xia, Catalytic activity origin and design principles of graphitic carbon nitride electrocatalysts for hydrogen evolution, Front. Mater. 6 (2019) 16, https://doi.org/10.3389/fmats.2019.00016.

[36] H.A. Hansen, J. Rossmeisl, J.K. Nørskov, Surface Pourbaix diagrams and oxygen reduction activity of Pt, Ag and Ni(111) surfaces studied by DFT, Phys. Chem. Chem. Phys. 10 (2008) 3722–3730, https://doi.org/10.1039/b803956a.

[37] J.K. Nørskov, J. Rossmeisl, A. Logadottir, L. Lindqvist, J.R. Kitchin, T. Bligaard, H. Jónsson, Origin of the overpotential for oxygen reduction at a fuel-cell cathode, J. Chem. Phys. 108 (46) (2004) 17886–17892, https://doi.org/10.1021/jp047349j.

[38] Y.-H. Lei, Z.-X. Chen, Density functional study of the stability of various α-Bi_2O_3 surfaces, J. Chem. Phys. 138 (2013) 054703, https://doi.org/10.1063/1.4788667.

[39] V. Wang, N. Xu, J.C. Liu, G. Tang, W.T. Geng, VASPKIT: a user-friendly interface facilitating high-throughput computing and analysis using VASP code, Comput. Phys. Commun. 267 (2021) 108033, https://doi.org/10.1016/j.cpc.2021.108033.

[40] G.W. Watson, S.C. Parker, G. Kresse, Ab initio calculation of the origin of the distortion of α-pbo, Phys. Rev. B 59 (13) (1999) 8481–8486, https://doi.org/10.1103/PhysRevB.59.8481.

[41] G.W. Watson, S.C. Parker, Origin of the Lone Pair of α-PbO from Density Functional Theory Calculations, J. Phys. Chem. B 103 (8) (1999) 1258–1262, https://doi.org/10.1021/jp9841337.

[42] A. Walsh, G.W. Watson, The origin of the stereochemically active Pb(II) lone pair: DFT calculations on PbO and PbS, J. Solid State Chem. 178 (5) (2005) 1422–1428, https://doi.org/10.1016/j.jssc.2005.01.030.

[43] A. Walsh, G.W. Watson, Influence of the anion on lone pair formation in Sn(II) monochalcogenides: a DFT study, J. Phys. Chem. B 109 (40) (2005) 18868–18875, https://doi.org/10.1021/jp051822r.

[44] D.O. Scanlon, A.B. Kehoe, G.W. Watson, M.O. Jones, W.I.F. David, D.J. Payne, R. G. Egdell, P.P. Edwards, A. Walsh, Nature of the band gap and origin of the conductivity of PbO_2 revealed by theory and experiment, Phys. Rev. Lett. 107 (24) (2011) 246402, https://doi.org/10.1103/PhysRevLett.107.246402.

[45] N.F. Quackenbush, J.P. Allen, D.O. Scanlon, S. Sallis, J.A. Hewlett, A.S. Nandur, B. Chen, K.E. Smith, C. Weiland, D.A. Fischer, J.C. Woicik, B.E. White, G. W. Watson, L.F.J. Piper, Origin of the bipolar doping behavior of SnO from X-ray spectroscopy and density functional theory, Chem. Mater. 25 (15) (2013) 3114–3123, https://doi.org/10.1021/cm401343a.

[46] A. Walsh, A.B. Kehoe, D.J. Temple, G.W. Watson, D.O. Scanlon, PbO_2: from semi-metal to transparent conducting oxide by defect chemistry control, Chem. Commun. 49 (5) (2013) 448–450, https://doi.org/10.1039/C2CC35928F.

[47] J.P. Allen, D.O. Scanlon, L.F.J. Piper, G.W. Watson, Understanding the defect chemistry of tin monoxide, J. Mater. Chem. C. 1 (48) (2013) 8194–8208, https://doi.org/10.1039/C3TC31863J.

[48] J.J. Carey, J.P. Allen, D.O. Scanlon, G.W. Watson, The electronic structure of the antimony chalcogenide series: Prospects for optoelectronic applications, J. Solid State Chem. 213 (2014) 116–125, https://doi.org/10.1016/j.jssc.2014.02.014.

[49] S.A. Razek, M.R. Popeil, Linda Wangoh, Jatinkumar Rana, Nuwanthi Suwandaratne, Justin L. Andrews, David F. Watson, Sarbajit Banerjee, Louis F.J. Piper, Designing catalysts for water splitting based on electronic structure considerations, Electron. Struct. 2 (2020) 023001, https://doi.org/10.1088/2516-1075/ab7d86.

[50] W. Guo, Y. Xie, Y. Liu, S. Shang, X. Lian, X. Liu, Effects of Sb_2O_3 polymorphism on the performances for electrocatalytic H_2O_2 production via the two-electron water oxidation reaction, Appl. Surf. Sci. 606 (2022) 155006, https://doi.org/10.1016/j.apsusc.2022.155006.

[51] A.S. Malik, T. Liu, M. Dupuis, R. Li, C. Li, Water oxidation on TiO_2: a comparative DFT study of 1e−, 2e−, and 4e− processes on rutile, anatase, and brookite, J. Phys. Chem. C. 124 (2020) 8094–8100, https://doi.org/10.1021/acs.jpcc.9b11450.

[52] G. Buvat, M.J. Eslamibidgoli, S. Garbarino, M.H. Eikerling, D. Guayl, OER performances of cationic substituted (100)-oriented IrO_2 thin films: a joint experimental and theoretical study, ACS Appl. Energy Mater. 3 (6) (2020) 5229–5237, https://doi.org/10.1021/acsaem.0c00069.

[53] R. Kishore, X. Cao, X. Zhang, A. Bieberle-Hütter, Electrochemical water oxidation on WO_3 surfaces: a density functional theory study, Catal. Today 321-322 (2019) 94–99, https://doi.org/10.1016/j.cattod.2018.02.030.

[54] X. Zhang, C. Cao, A. Bieberle-Hütter, Orientation sensitivity of oxygen evolution reaction on hematite, J. Phys. Chem. C. 120 (50) (2016) 28694–28700, https://doi.org/10.1021/acs.jpcc.6b10553.

[55] M. García-Mota, M. Bajdich, V. Viswanathan, A. Vojvodic, A.T. Bell, J.K. Nørskov, Importance of correlation in determining electrocatalytic oxygen evolution activity on cobalt oxides, J. Phys. Chem. C. 116 (39) (2012) 21077–21082, https://doi.org/10.1021/jp306303y.

[56] Q. Liang, G. Brocks, V. Sinha, A. Bieberle-Hütter, Tailoring the performance of ZnO for oxygen evolution by effective transition metal doping, ChemSusChem 14 (2021) 1–11, https://doi.org/10.1002/cssc.202100715.

[57] Y.-F. Li, Z.-P. Liu, Active site revealed for water oxidation on electrochemically induced δ-MnO_2: role of spinel-to-layer phase transition, J. Am. Chem. Soc. 140 (5) (2018) 1783–1792, https://doi.org/10.1021/jacs.7b11393.

[58] J. Zhu, L. Hu, P. Zhao, L.Y.S. Lee, K.-Y. Wong, Recent advances in electrocatalytic hydrogen evolution using nanoparticles, Chem. Rev. 120 (2) (2020) 851–918, https://doi.org/10.1021/acs.chemrev.9b00248.

[59] J.K. Nørskov, T. Bligaard, A. Logadottir, J.R. Kitchin, J.G. Chen, S. Pandelov, U. Stimming, Trends in the exchange current for hydrogen evolution, J. Electrochem. Soc. 152 (3) (2005) J23–J26, https://doi.org/10.1149/1.1856988.
[60] Y.H. Li, P.F. Liu, L.F. Pan, H.F. Wang, Z.Z. Yang, L.R. Zheng, P. Hu, H.J. Zhao, L. Gu, H.G. Yang, Local atomic structure modulations activate metal oxide as electrocatalyst for hydrogen evolution in acidic water, Nat. Commun. 6 (2015) 8064, https://doi.org/10.1038/ncomms9064.
[61] B.G. Ghule, J.-H. Jang, Determining the effect of cation (Ti/Zr) doping in bismuth oxide for electrochemical CO2 reduction to formic acid: a DFT Study, Energy Fuels 37 (23) (2023) 18009–18018, https://doi.org/10.1021/acs.energyfuels.3c01722.
[62] P. Jiang, Y. Yang, R. Shi, G. Xia, J. Chen, J. Su, Q. Chen, Pt-like electrocatalytic behavior of Ru–MoO_2 nanocomposites for the hydrogen evolution reaction, J. Mater. Chem. A 5 (2017) 5475–5485, https://doi.org/10.1039/C6TA09994G.
[63] L. Li, G. Zhang, G. Yang, T. Yang, S. Yang, S. Yang, Electrochemically modifying the electronic structure of IrO_2 nanoparticles for overall electrochemical water splitting with extensive adaptability, Adv. Energy Mater. 10 (30) (2020) 2001600, https://doi.org/10.1002/aenm.202001600.
[64] N. Wang, S. Ning, X. Yu, D. Chen, Z. Li, J. Xu, H. Meng, D. Zhao, L. Li, Q. Liu, B. Lu, S. Chen, Graphene composite with Ru-RuO_2 heterostructures: highly efficient Mott-Shottky-type electrocatalysts for pH-universal water splitting and flexible zinc-air betteries, Appl. Catal. B Environ. 302 (2022) 120838, https://doi.org/10.1016/j.apcatb.2021.120838.
[65] B. Ren, Q. Jin, Y. Li, H. Cui, C. Wang, Activating titanium dioxide as a new efficient electrocatalyst: from theory to experiment, ACS Appl. Mater. Interfaces 12 (10) (2020) 11607–11615, https://doi.org/10.1021/acsami.9b21575.
[66] Y. Ma, P. Ou, Z. Wang, A. Zhu, L. Lu, Y. Zhang, W. Zeng, J. Song, J. Pan, Interface engineering in CeO_2 (1 1 1) facets decorated with CdSe quantum dots for photocatalytic hydrogen evolution, J. Colloid Interface Sci. 579 (1) (2020) 707–713, https://doi.org/10.1016/j.jcis.2020.06.100.
[67] Defect-engineered ultrathin δ-MnO_2 nanosheet arrays as bifunctional electrodes for efficient overall water splitting, Adv. Energy Mater. 7 (18) (2017) 1700005, https://doi.org/10.1002/aenm.201700005.
[68] Z.A. Shaikh, S.D. Raut, H.M. Danamaha, C. Kamble, P.V. Shinde, S.F. Shaikh, S. S. Mohite, H.A. Barve, K.C. Gunturu, R.S. Mane, Solution-processed Sb_2O_3: a promising electrode material for high-performance supercapacitors and electrocatalysts, J. Enenrgy Storage 89 (2024) 111736, https://doi.org/10.1016/j.est.2024.111736.